Frequency-Selective Transition from Substrate-Integrated-Waveguide to Rectangular Waveguides for 77/130 GHz Automotive Radar Using

Citation for the original published paper (version of record):
Van Hastenberg, K., Ivashina, M., Bart Smolders, A. et al (2026). Frequency-Selective Transition from Substrate-Integrated-Waveguide to Rectangular Waveguides for 77/130 GHz Automotive Radar Using Metal-Only Additive Manufacturing. IEEE Transactions on Components, Packaging and Manufacturing Technology, 16(8): 1881-1893.
http://dx.doi.org/10.1109/TCPMT.2026.3697854

(article starts on next page)

Frequency-Selective Transition From Substrate-Integrated-Waveguide to Rectangular Waveguides for 77/130-GHz Automotive Radar Using Metal-Only Additive Manufacturing

Kevin A. P. van Hastenberg, *Graduate Student Member, IEEE*, Marianna V. Ivashina, *Senior Member, IEEE*, A. Bart Smolders, *Senior Member, IEEE*, and Artem R. Vilenskiy, *Senior Member, IEEE*

***Abstract*—This article presents a compact dual-band substrate integrated waveguide (SIW)-to-rectangular waveguide (RWG) frequency-selective transition (FST). This FST is a key enabler of future dual-band systems, such as automotive radar operating at 77 and 130 GHz. The proposed structure enables efficient signal routing from a single beamforming integrated circuit (BFIC) to two separate antenna arrays, leveraging waveguide (WG)-based filtering for high-frequency integration. A vertical transition topology is adopted to enhance mechanical robustness and to simplify assembly. This robustness is validated by performing a sensitivity analysis on the assembly. The structure is fabricated using aluminum-based laser powder-bed fusion (LPBF), enabling monolithic integration of complex millimeter-wave (mmWave) features. Experimental results demonstrate insertion loss (IL) around 2.5 dB for the low and high bands of the FST, with measured isolation exceeding 30 dB in the high band. The results validate the feasibility of the proposed FST and highlight the impact of manufacturing tolerances on mmWave performance. This work contributes a scalable, low-loss packaging solution for dual-band radar front ends in next-generation automotive and 6G sensing applications.**

***Index Terms*—Diplexer, dual-frequency, millimeter-wave (mmWave), substrate-integrated waveguide (SIW), transition, waveguide (WG) filter.**

I. Introduction

As AUTONOMOUS driving and intelligent transportation systems advance, radar technologies are evolving rapidly to meet new sensing requirements. JCAS systems are gaining increased attention, especially within the proposed 6G spectrum, where additional bandwidth is being allocated for automotive radar in the D-band around 130-GHz [1]. This higher frequency band enables finer spatial resolution and more accurate environmental mapping due to the 1–7 GHz of available bandwidth [2]. Moreover, the 130-GHz band is expected to be less impacted by interference from unlicensed WLAN systems than lower millimeter-wave (mmWave) bands [3]. However, due to increased free-space path loss at 130 GHz, it is less suitable for long-range detection and is better suited as a complementary radar system rather than a full replacement for existing 77 GHz systems. Combining both bands in a dual-frequency radar system offers enhanced performance by leveraging the strengths of each frequency. In addition, the restricted available sensor space (often $< 90 \times 70 \times 20$ mm^3 [4]) can be shared between the two systems, resulting in a higher space efficiency.

Designing dual-band radar systems introduces several challenges. First, antenna array design is constrained by the need to avoid grating lobes, which requires near-free-space half-wavelength interelement spacing at the highest frequency. This conflicts with the antenna size, which is often the effective half-wavelength at the lowest frequency. The challenge becomes more pronounced when the two operating frequencies are widely spaced, as the optimal array geometries for each band differ significantly. A practical solution is to split the output of a dual-band beamforming integrated circuit (BFIC) into two separate arrays optimized for each frequency.

Second, integrating mmWave radar electronics with antennas involves significant interconnect and routing losses. Conventional transitions such as solder balls [5] and bondwires [6] introduce substantial insertion loss (IL), especially at higher frequencies. Moreover, printed circuit board (PCB)-like processes exhibit significant routing losses due to the inherently lossy nature of transmission lines, and vertical interconnects such as vias further add to cost and increased losses. For front-facing automotive radar, the required maximum effective isotropic radiated power (EIRP) will be in between 20–40 dBm [2] at 130 GHz. Due to the limited power amplifier (PA) output power at these frequencies, minimizing interconnect losses is of utmost importance.

Received 23 December 2025; revised 21 April 2026; accepted 24 May 2026. Date of publication 28 May 2026; date of current version 27 August 2026. This work was supported by the Dutch Research Council [Nederlandse Organisatie voor Wetenschappelijk Onderzoek (NWO)] through Research Program Share-Waves under Project 19469. The work of Marianna V. Ivashina and Artem R. Vilenskiy was supported by Sweden-Taiwan Collaborative Research Framework Project "Antenna Technologies for Beyond-5G Wireless Communication" from Swedish Foundation for Strategic Research. Recommended for publication by Associate Editor X. Gu upon evaluation of reviewers' comments. *(Corresponding author: Kevin A. P. van Hastenberg.)*

Kevin A. P. van Hastenberg and A. Bart Smolders are with the Electromagnetics Group, Department of Electrical Engineering, Eindhoven University of Technology, 5612 Eindhoven, The Netherlands (e-mail: k.a.p.v.hastenberg@tue.nl).

Marianna V. Ivashina is with the Antenna Group, Department of Electrical Engineering, Chalmers University of Technology, 412 96 Gothenburg, Sweden.

Artem R. Vilenskiy was with the Department of Electrical Engineering, Chalmers University of Technology, 412 96 Gothenburg, Sweden. He is now with the XPANCEO Research on Natural Science, Dubai, United Arab Emirates.

Digital Object Identifier 10.1109/TCPMT.2026.3697854

Various transition structures have been proposed to address these challenges, including ridge waveguide (WG) to silicon chip transitions [7], substrate integrated waveguide (SIW)-to-microstrip transitions [8], [9], and coplanar WG-based designs [10]. While these demonstrate feasibility, they typically target single-band operation and lack integration with diplexing functionality. Notably, Erkelenz et al. proposed two concepts: one that diplexes two bands in a rectangular waveguide (RWG) to grounded coplanar WGs [11], and another that transitions from RWG to multiple SIWs acting as a frequency-selective power splitter and transition [12]. Both operate at 20–30 GHz. However, extending these concepts to dual-band frequency-selective packaging is nontrivial due to competing constraints on bandwidth, isolation, and mechanical assembly. Furthermore, practical realizations at 77/130 GHz must account for manufacturing-driven effects such as surface roughness, dimensional tolerances, and assembly misalignment, which can dominate the performance at these high frequencies.

Metal-only additive manufacturing, and in particular laser powder-bed fusion (LPBF), offers an attractive path toward monolithic WG packaging with integrated RF features, reduced part count, and simplified assembly. At the same time, LPBF introduces constraints on printable geometry and brings tolerance- and roughness-related uncertainties that require dedicated design-for-manufacturing and experimental validation at mmWave frequencies.

This article introduces a dual-frequency SIW-to-RWG frequency-selective transition (FST) operating at 77 and 130 GHz, realized using metal-only LPBF and validated experimentally. To the author's best knowledge, this article is the only one to address such a high frequency for an FST. The proposed transition not only supports the integration of BFICs and antenna arrays but also incorporates frequency-splitting functionality. This integration simplifies the overall architecture and reduces IL by eliminating the need for separate filtering components. A preliminary study of the underlying concept and related challenges was reported in our initial work in [13]. The present article substantially extends that work by introducing a fundamental analysis and a manufacturable realization framework, together with experimental verification on an additively manufactured prototype. The main contributions of this work are summarized as follows: 1) a compact dual-band FST integrating diplexing functionality directly into an SIW-to-RWG transition for 77/130-GHz automotive radar systems; 2) a simplified circuit-level model that describes the FST operation and identifies the critical parameters governing frequency selectivity, matching, and isolation; 3) a design flow that uses metal-only LPBF to realize complex 3-D mmWave WG structures with monolithic integration of filtering features; and 4) an experimental validation, together with an analysis of the dominant fabrication- and assembly-induced sensitivities affecting the realized performance.

The remainder of this article is organized as follows. Section II describes the general system-level integration concepts and introduces the key definitions and performance goals. Section III presents the circuit model and introduces the key concepts, followed by the design procedure in Section IV. Experimental results are provided in Section V, and the discussion and conclusion are presented in Sections VI and VII, respectively.

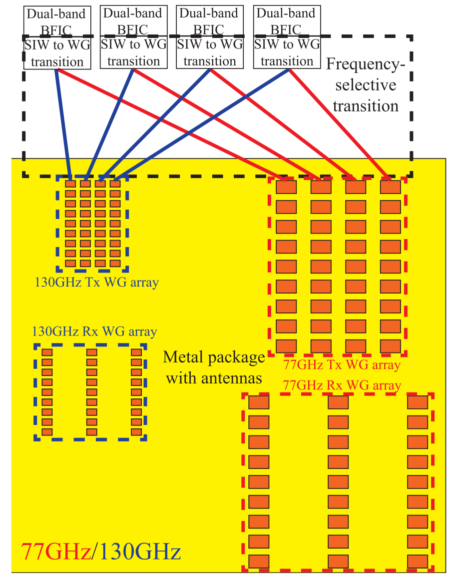

Fig. 1. Use-case scenario of the proposed FST for dual-band WG arrays. Only Tx BFICs are shown. Not to scale.

II. System-Level Integration Concept

Fig. 1 introduces a novel system-level integration concept enabled by the proposed dual-band FST. The focus is on architectural implications for dual-frequency automotive radar front ends, rather than on geometry-level design implementation details, which are addressed later in Fig. 2. In this use-case scenario, a common dual-band BFIC powers two separate WG antenna arrays, one for 77 GHz and one for 130 GHz, via a shared FST. The antennas are embedded within a metal package, enabling low-loss WG-based RF routing. This packaging approach eliminates the need for lossy PCB-based transmission lines, solder balls, or bondwires to feed the antennas. The proposed FST structure connects the BFIC to the WG arrays through a compact SIW-to-RWG interface that simultaneously performs frequency splitting using a low-pass filter (LPF) in the low-band channel and a below-cutoff RWG in the high-band channel. This allows the dual-band signal from the BFIC to be efficiently split and routed to the appropriate antenna array, minimizing IL and maximizing integration density. Compared to implementing two independent radar front-ends, the proposed architecture is particularly advantageous in packaging-constrained dual-band modules where a shared aperture and a common dual-band BFIC are available or desired. In this use case, the RF back-end is consolidated into a single BFIC, while the band separation is shifted into a passive, package-integrated transition. This reduces duplication of mmWave front-end resources and, critically, the number of high-frequency interconnects and feedthroughs, which often dominate area and assembly effort in tightly integrated modules. Since the FST is realized as a compact,

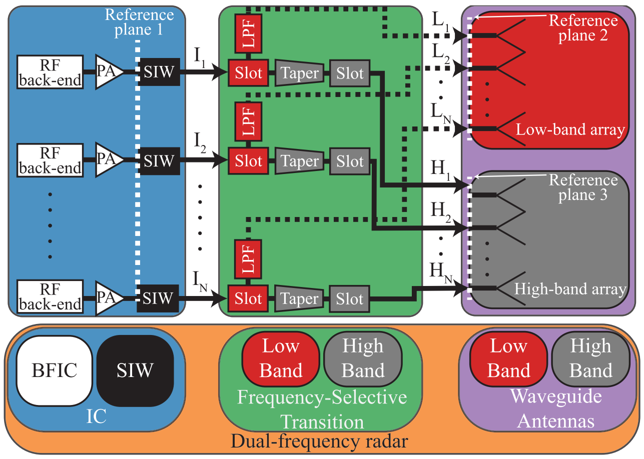

Fig. 2. Block diagram of the proposed frequency-selective transition in a dual-band radar transmit system (the same concept can also be used in a receive system). Low-band is for operation in the WR-10 band around 77 GHz; high-band is for operation in the WR-8 band around 130 GHz. Each FST has an input (I_x) and an output for the low-band (L_x) and high-band (H_x). Reference planes 1,2,3 correspond to Port 1,2,3, respectively.

passive SIW-to-RWG feature inside the metal package, the incremental integration overhead is small compared to duplicating complete RF channels and their packaging interfaces. Consequently, the FST trades one passive three-port network for a net reduction in footprint, RF routing complexity, and integration risk in shared-aperture, dual-band radar modules.

Fig. 2 details the implementation of the FST in the complete system. The FST is a three-port passive network with one SIW port (Reference plane 1) and two RWG ports (Reference planes 2 and 3), placed between the BFIC and the two antenna apertures.

The topology in Fig. 2. implements the proposed FST by co-routing the SIW port into two physically distinct paths. A slot-coupled junction (the red-colored "Slot" block in the FST path in Fig. 2) realizes the SIW-RWG transition. The frequency-selectivity of the FST is created by design

1) *Low-Band (77 GHz) Path:* A compact RWG-based LPF is inserted to reject high-frequency spectral components, ensuring only 77 GHz is transmitted toward Reference plane 2.
2) *High-Band (130 GHz) Path:* A tapered SIW and RWG providing below-cutoff operation for the low-frequency spectral components inherently filtering these, while also providing low-loss transmission of high-frequency signals toward Reference plane 3.

While the antennas are physically isolated (see Fig. 1), finite cross-band isolation can lead to signal leakage between transmit paths. For instance, 10 dB isolation implies that a typical 10 dBm signal at 77 GHz couples as 0 dBm into the 130-GHz path. Although this coupled power is not radiated efficiently due to a mismatch at the antenna port, it may introduce unwanted intermodulation, lower radiation efficiency, or decrease the carrier-to-interference ratio. Therefore, high isolation is critical in dual-frequency radar systems. While in some works [14] the cross-band isolation is greater than 35 dB, this will not be targeted in this publication mainly due to the absence of integrated antennas in this publication, which would add to the frequency-selectivity of the two paths in the FST. If stronger low-band rejection in the high-band channel is required, an explicit high-pass filter (HPF) can be inserted without changing the proposed FST synthesis. Alternatively, the below cut-off RWG can be elongated at the cost of increased IL in the high band.

III. Methodology

A. Transitions

As explained in the introduction, wire bonding and solder balls suffer from high IL at mmWave frequencies [6]. An emerging alternative is to print transmission line ramps directly from the die to a carrier, as demonstrated in [15], which shows promise beyond 100 GHz. However, this technology is not yet readily available and is limited to thin dies (50 μm thickness was used in this publication).

Above 60 GHz, SIWs have shown superior performance over microstrip and coplanar lines in terms of IL and shielding, making them attractive for on-carrier signal routing. To further guide signals to external WG-based antennas, a transition from SIW to a RWG becomes necessary. In this work, we explore such a transition from a SIW to a RWG.

Two main types of SIW-to-RWG transitions exist: transverse (inline) and vertical (orthogonal). Transverse transitions, such as those in [10], [16], and [17], are often embedded in split-block assemblies and are prone to leakage, alignment errors, and complex assembly. These transitions are usually constructed by launching a mode in the RWG directly from an open-ended SIW. Vertical transitions, as seen in [8], [9], [18], and [19], typically use transverse slots in SIW broad walls and offer better mechanical robustness and integration simplicity due to leveraging the z dimension as well, allowing stacked designs.

For the presented FST, a vertical transition topology using broad wall coupling slots is selected for its mechanical simplicity, alignment tolerance, and compatibility with metal packaging.

B. Diplexers

A diplexer enables the separation of two frequency bands from a common port, allowing a single BFIC to feed two distinct antenna arrays. Diplexers are typically realized using bandpass and LPF/HPF combinations, implemented in WG, microstrip, or SIW technologies. However, in this publication the diplexer consists of an LPF and below-cutoff sections, as can be seen in Fig. 2.

Recent literature has explored various compact and high-performance diplexer designs suitable for mmWave applications. Hung et al. [20] proposed a miniaturized dual-band diplexer using substrate-integrated coaxial cavity resonators, achieving high isolation and low IL. These are key requirements for automotive radar integration. Huang et al. [21] introduced a wideband hybrid diplexer operating in the D-band (110–134 GHz and 146–170 GHz), using high-low pass filters and hybrid couplers to achieve over 100 dB isolation and sub-0.5 dB IL, demonstrating feasibility for 6G radar and sensing systems. These works emphasize the trend toward embedding filtering functionality directly into compact RF structures to reduce complexity and improve performance.

C. RWG, SIW and LPF Description

The characteristic impedance (*P-I* definition) of the WGs, supporting the fundamental TE_{10} modes, is given by [22] and [23]

$$Z = \frac{Z^{\infty}}{\sqrt{1-\left(\frac{f_c}{f}\right)^2}} \tag{1}$$

with Z^{∞} the high-frequency impedance asymptotics and f_c the mode cut-off frequency described as follows:

$$Z^{\infty} = \frac{\pi^2}{8}\frac{120\pi}{\sqrt{\epsilon_r}}\frac{H}{W'}, \quad f_c = \frac{c_0}{2W'\sqrt{\epsilon_r}}. \tag{2}$$

Here, ϵ_r is the relative permittivity, c_0 is the speed of light in vacuum, H is the height of the WG, and W' is the effective width of the WG. This effective width is the physical width for an air-filled WG and is described by $W'_{SIW} = W_{SIW} - D^2/0.95P$ for the SIW, where D and P are the SIW sidewall via diameter and period [24], respectively.

The LPF in the 77-GHz path is essential for suppressing unwanted high-frequency spectral components from the dual-band input. It ensures that only the 77-GHz signal reaches the low-band WG output, enabling effective frequency splitting within the transition structure.

A fourth-order Chebyshev design was selected to achieve a sufficient stopband rejection while maintaining a compact footprint, as will be detailed in Section IV-B. This choice reflects a tradeoff between isolation and size: higher order filters offer better isolation but introduce more impedance transitions, which can increase IL at the passband.

D. Equivalent Circuit-Level Model

A simplified hybrid circuit model treats the structure in Fig. 2 as a combination of cascaded WG transmission line sections, SIW-to-RWG transition lumped equivalents, and the Chebyshev LPF two-port network. The model can be used to investigate the following tradeoffs.

1) *Chebyshev LPF order versus Isolation:* Lower filter orders reduce filter selectivity, potentially increasing leakage between bands. However, the passband losses increase with a higher filter order.
2) *Transition length versus Loss:* Shorter SIW and RWG reduce loss but may introduce impedance mismatches and degraded isolation.

The circuit model is presented in Fig. 3. Standard RWG sections are used with different relative permittivities corresponding to the air-filled RWGs and the SIWs. Two different transition mechanisms are used: an electrically narrow coupling transverse slot in the SIW broad wall for the 77-GHz path, and an *E*-plane RWG bend for the 130-GHz path (slot size similar to RWG dimension). The low band slot is modeled as two parallel *LC* resonators coupled through an impedance transformer [25]. The *E*-plane bend and the taper in the SIW

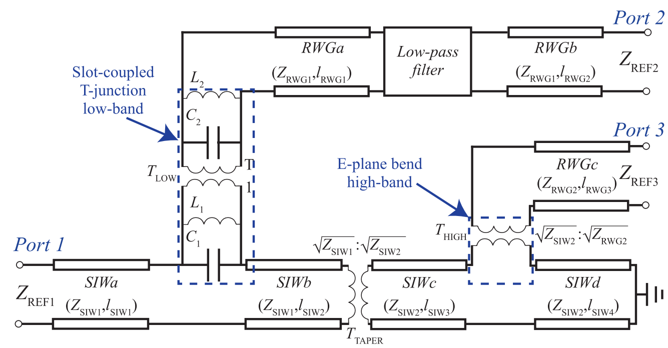

Fig. 3. Circuit model of the proposed FST in Fig. 2. The transition to the low-band output (Port 2) is achieved using a slot-coupled T-junction. Both the taper and high-band *E*-plane bend are modeled as ideal impedance transformers and form the path toward the high-band output (Port 3). SIW_c, SIW_d and RWG_c create a below-cutoff path for the low-frequency spectral components, inherently filtering these.

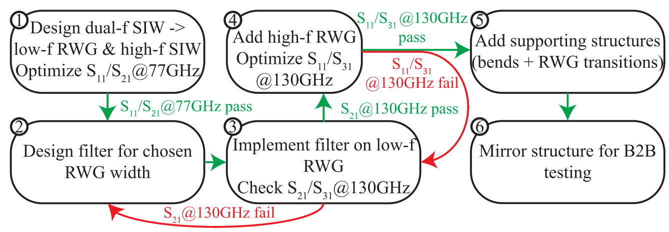

Fig. 4. Design procedure for an FST. The red arrows signify a feedback loop when design requirements are not met, whereas the green arrows indicate a pass on these design requirements.

section are both modeled using ideal impedance transformers [26]. To have an accurate LPF representation, the filter was synthesized numerically using full-wave simulation (in CST Studio Suite 2025 [27]) (in Section IV-B), after which its two-port S-matrix was imported into the circuit model.

IV. Design Procedure

The design procedure to build an FST as described in Fig. 2 is shown in Fig. 4. It starts from designing the dual-band (or wideband) SIW with a single transition to the low-band RWG output. After adding a filter, the second transition to the RWG high-band output and the supporting structures, the whole FST can be constructed. In steps 3 and 4, feedback loops provide places to optimize the desired parameters for the design. Following this design procedure allows one to design an FST with minimal losses, taking into account the specific process design rules for the intended manufacturing. In this project, LPBF is used, which will be discussed in more detail in Section IV-A.

The FST is targeted for the automotive bands at 77 and 130 GHz. A bandwidth (BW) of 5 and 20 GHz is envisioned for these two bands, respectively. A transition loss of < 2 dB is desired for both bands, which is challenging given the high-frequency implementation and additional requirements on interband isolation. This section covers the LPF synthesis (step 2) in Section IV-B, the results of the analytical model (step 4) in Section IV-C, the complete single-ended FST (step 5) in Section IV-D, and its sensitivity analysis in

Fig. 5. X-ray image of a manufactured prototype for an old design, depicting artifacts close to the RWG channels. Due to these artifacts, the preferred minimum resolution was increased from 100 to 200 μm.

Section IV-E. Finally, the back-to-back (B2B) design (step 6) is described in Section IV-F.

A. Manufacturing Technology

The metal WG block prototypes were manufactured using all-metal 3-D printing technology with AlSi10Mg [28], which is well-suited for additive processes due to its good thermal conductivity, mechanical strength, and printability. In particular, the structures are fabricated using LPBF, a metal 3-D printing technique that builds parts layer-by-layer, enabling the realization of complex internal geometries that would be difficult or impossible to achieve using conventional computer numerical control (CNC) machining.

Compared to traditional CNC-milling of split-block WG assemblies, LPBF offers several advantages. Split-block milling requires precise alignment and assembly, and is limited in terms of internal routing complexity. While it provides excellent surface finish and dimensional accuracy, it is less suitable for compact, integrated multifunctional structures like the one proposed in this work. Monolithic 3-D printing like LPBF, on the other hand, eliminates assembly steps and allows for seamless integration of transitions, filters, and WGs in a single part. This reduces parasitic effects from split-block interconnects and misalignments, supporting more compact and robust designs.

However, LPBF also introduces challenges. One of the main limitations is the relatively high surface roughness (SR), which can significantly impact mmWave performance. The as-printed rms SR for LPBF is typically 6 $\pm$ 2 μm, which can be improved to 4 $\pm$ 1 μm through postprocessing such as glass bead blasting [29]. While this is still rougher than machined surfaces, it can be mitigated through careful design and simulation of associated loss mechanisms.

X-ray imaging is used to inspect the internal structures of the test printed parts. Fig. 5 shows an X-ray image of a first-generation prototype, previously presented in [13]. Small air gaps are visible between the WG walls and surrounding metal. The cause of these voids is still under investigation, but the internal geometry remains intact. Based on this experience, the preferred minimum feature size in the current design was increased from 100 to 200 μm to improve print reliability and reduce the risk of incomplete material fusion. Moreover, RWG channels were separated sufficiently to avoid voids between them.

For prototyping purposes, the BFIC interface is emulated using a PCB-based SIW structure. This allows for practical validation of the FST behavior before integrating with actual BFICs. In this study, a Rogers 0.508-mm thick RO4003C substrate is used (ϵ_r = 3.55, $\tan\delta$ = 0.0027) with 35 μm tin-plated copper.

B. LPF Synthesis (Step 2)

As discussed in Sections III-C and III-B, the LPF is a key component enabling frequency-splitting by suppressing high-frequency signals in the 77-GHz path. The design, shown in Fig. 6, consists of five capacitive irises and four resonant cavities, forming a fourth-order Chebyshev filter. This topology was selected to balance stopband attenuation, compactness, and manufacturability.

To comply with the LPBF manufacturing constraints, a taper was added on the SIW input side to transition between WG heights without violating the minimum printable feature size of 200 μm. On the output side, such a taper was not feasible due to impedance mismatches, resulting in a 150 μm step.

Simulation results in Fig. 7 confirm the targeted performance: a reflection coefficient better than −15 dB at 77 GHz, a −10 dB bandwidth of 12 GHz, and an IL of approximately 1.2 dB in the passband. In the stopband (120–140 GHz), the filter achieves at least 32 dB suppression, validating its objective to isolate the high-frequency signal.

C. Results of Analytical Model (Step 4)

This section highlights the results of the model introduced in Section III-D and corresponds to step 4 in Fig. 4. The model includes both dielectric losses for the SIWs and the metal conductivity for copper and aluminum for the SIWs and RWGs. The model, however, does not include additional loss mechanisms like the SR effect. In the model, the previously designed LPF is used as a two-port S-parameter block to predict the behavior of the whole structure accurately.

Optimizing the values using advanced design system [30] resulted in the S-parameters shown in Fig. 8. As the height of the SIW sections was fixed by the PCB material, only the width determined the relevant impedance. The widths for Z_{SIW1} and Z_{SIW2} are 1.45 and 0.98 mm, respectively. The relevant lengths for the SIW are the length between the two slots (including taper) $L_{\mathrm{SIW2}} + L_{\mathrm{SIW3}}$ = 1.72 mm and the termination of the high-band SIW L_{SIW4} = 0.27 mm.

For the RWG, the widths of the WGs were fixed at the standardized WG widths of 2.032 and 2.54 mm, for WR-8 and WR-10, respectively. The heights of the RWG at *RWGa* and *RWGc* (see Fig. 3) are 0.45 and 0.25 mm, respectively. These widths result in the correct impedances to match these sections to the slots in the SIWs.

The simulations show that it is possible to create a transition using our concept, which splits both bands to separate RWG output ports with a large BW and decent isolation. The isolation in the high band is a lot better compared with the

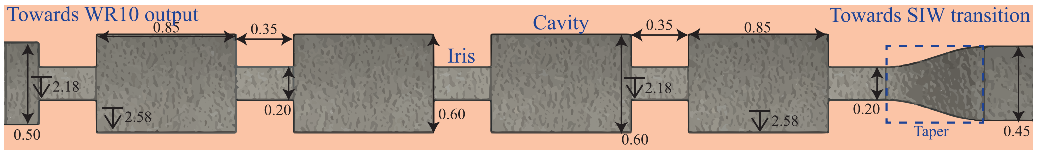

Fig. 6. Geometry of the RWG LPF for blocking high-frequency signals (Step 2 of design procedure in Fig. 4). The filter consists of four cavities and four irises and uses a tapered section on the right to account for the resolution of the manufacturing process. All dimensions in mm.

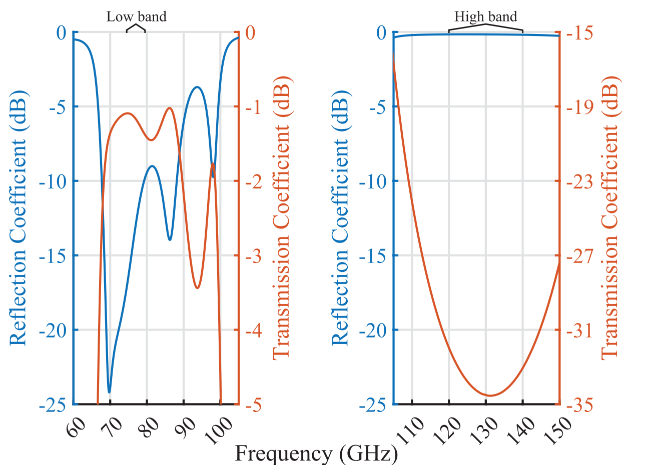

Fig. 7. Simulation results of the LPF shown in Fig. 6 (Step 2 of design procedure in Fig. 4) showing over 10 GHz of BW in the low band with IL around 1.5 dB. The transmission coefficient in the high band is below −31 dB, providing sufficient filtering.

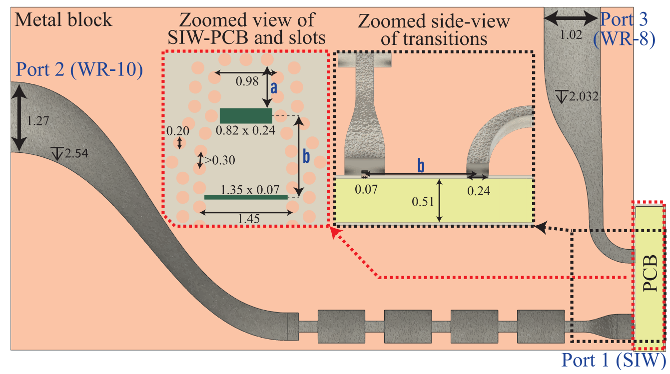

Fig. 9. Schematic of single-ended transition (Step 5 of design procedure in Fig. 4) showing the metal printed part and the SIW on PCB. Detailed view of the LPF is shown in Fig. 6. *a* (the tuning of the short, around half-wavelength) and *b* (distance between the two coupling slots) parameters signify important tuning parameters highlighted in this section. All dimensions in mm.

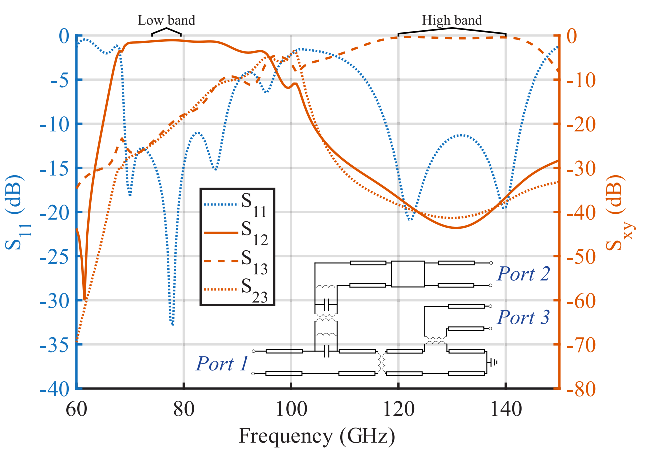

Fig. 8. Simulated S-parameters of the optimized parameters using the analytical model shown in Fig. 3 (Step 4 of design procedure in Fig. 4). These results show a wide BW in both the low- and high-band with losses less than 1 dB.

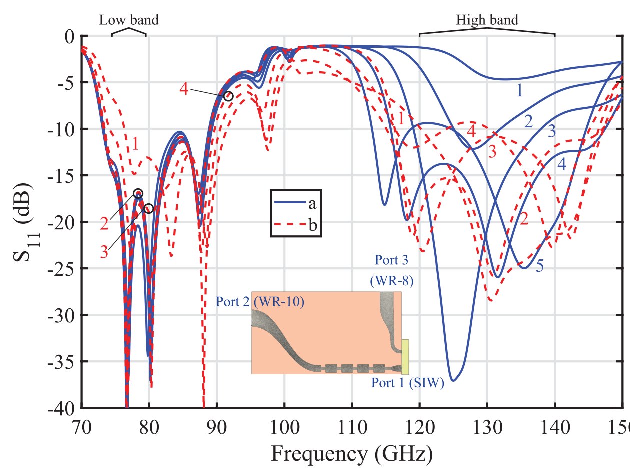

Fig. 10. Parameter sweeps for parameter *a* and *b* in the single FST shown in Fig. 9 (Step 5 of design procedure in Fig. 4). Parameter *a* from line 1 to 5: [0.6, 0.7, 0.8, 0.9, 1] mm, Parameter *b* is fixed at 1.27 mm. Parameter *b* from line 4 to 5: [0.6, 1.27, 0.8, 1] mm, Parameter *a* is fixed at 0.88 mm.

low band due to the LPF in the low-band path. Possibly, improvements can be made by implementing a dedicated HPF in the high-band path or simply elongating the narrow SIW or RWG sections. This will, however, lead to a higher passband IL. Furthermore, higher isolation toward the high-band port results in a narrower BW in this band as well. Moreover, the inter-output isolation S_{23} aligns closely with S_{13} in the low band and S_{23} in the high band, provided by the low-loss nature of the FST, having impedance-matched input and output ports. This results in the main focus in the remainder of this article toward optimizing the S_{12} and S_{13}.

D. Single-Ended FST (Step 5)

The single-ended FST integrates the SIW-to-RWG interface and the LPF into a compact structure. As described in Section III-C, the RWG dimensions were optimized using 1 and the analytical model to match the SIW impedance. The resulting RWG heights are 0.44 mm for the low band and 0.25 mm for the high band. After the transition, these taper to the standard WR-10 and WR-8 interfaces, respectively. The WR-8 RWG provides natural high-pass filtering close to the cut-off frequency of 73.77 GHz (2).

The SIW widths were set to 1.45 and 0.98 mm (via center-to-center) for the low and high bands, using a height of 0.508

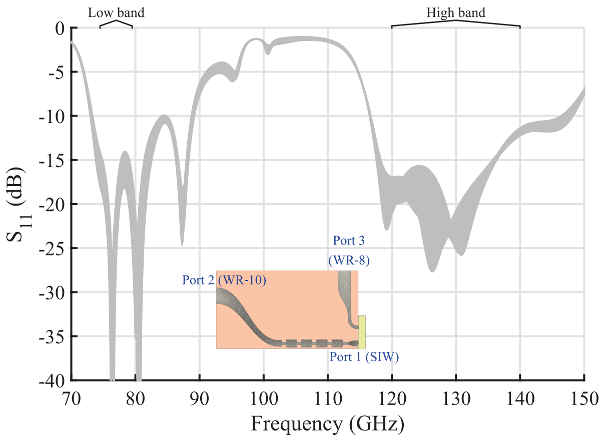

Fig. 11. Sensitivity analysis for the PCB placement on the single-ended FST shown in Fig. 9 simulated for the common input port. x-error: –20 to 20 μm, y-error: –20 to 20 μm and z-error: 0 to –20 μm. The plot includes the combined worst error (x-error: −20 μm, y-error: −20 μm, z-error: −20 μm). These results show that the design is robust against these PCB alignment errors.

mm. A double row of 200 μm-diameter vias with 300 μm spacing was used to suppress leakage, particularly for the high-frequency band.

The low-band slot is 1.35 $\times$ 0.07 mm while in the high-band a slot of 0.82 $\times$ 0.24 mm is used. The SIW end is short-circuited at a distance a (L_{SIW4} in the analytical model) approximately half wavelength from the high-frequency coupling slot, while the distance between the two slots is denoted as b ($L_{\mathrm{SIW2}} + L_{\mathrm{SIW3}}$ in the analytical model). These parameters are critical tuning variables and were optimized using full-wave simulations to minimize reflection and maximize isolation. The single FST is shown in Fig. 9 and is previously discussed in more detail in [13].

To indicate the importance of a and b, parameter sweep graphs are shown in Fig. 10. First, the parameter a is used to define an optimal short-circuit plane position. A value deemed to provide a sufficient bandwidth and matching was found to be 0.88 mm. Second, the parameter b was swept, which was used to further tune the low- and high-band. A value of 1.27 mm was found to be optimal.

E. Assembly Sensitivity

To validate the robustness of the design against assembly tolerances, a sensitivity analysis was performed in CST. The simulation, shown in Fig. 11, evaluates the impact of misalignments in the x, y, and z directions between the metal block and the PCB shown in Fig. 9. Even under the worst-case combined error ($x = -20$ μm, $y = -20$ μm, and $z = -20$ μm), the transition performance maintains acceptable, though with a slight narrowing of the bandwidth in the low band. The largest contribution to the error is caused by the z error, which quickly causes leakage in the high band, lowering the transmission coefficient. To minimize assembly errors, alignment pins were added to the metal block.

F. B2B FST Validation (Step 6)

To facilitate measurement and validation, a B2B prototype was developed. This configuration allows the use of the standardized WR-10 and WR-8 WG interfaces on both sides of the structure. A detailed schematic is shown in Fig. 12.

The PCB is mounted using six screws and two alignment pins. A tight tolerance on the alignment pins ensures accurate positioning of the PCB relative to the metal block, minimizing the impact of misalignment, as discussed in the sensitivity analysis. Additionally, the PCB is seated in a 200 μm deep recessed cavity for shielding and mechanical stability. To ensure flat contact and reduce variability, the contact areas are raised on 100 μm high platforms, visible in the lower left zoomed-in view of Fig. 12.

V. Results

A. Measurement Setup

To evaluate the performance of the proposed FST, two dedicated measurement setups were used for the WR-10 and WR-8 bands, respectively, as shown in Fig. 13. The WR-10 band was measured using WR-12 vector network analyzer (VNA) extenders with WR-10 to WR-12 transitions. Due to the absence of a WR-10 calibration kit, a WR-12 calibration kit was used, and a normalization plane (green line) was introduced to de-embed the WR-10 to WR-12 transition influence. For the WR-8 band, WR-8 VNA extenders were used directly, with calibration planes indicated in red.

To ensure proper termination of unused ports, horn antennas with reflection coefficients of at least −20 dB were employed to radiate into absorbers, minimizing reflections and ensuring accurate S-parameter measurements.

While some of these setups involved RWGs excited below cutoff or outside of the single-mode regime, the measurements showed good alignment with the simulations. Especially, exiting the RWG outside the single-mode regime can cause some accuracy problems in the measurement. Nevertheless, in the simulation, the second-order mode did not propagate through the structure.

B. B2B RWG Characterization

To isolate the performance of the RWG channels from the full transition structure, two B2B blocks were fabricated and measured—one for each frequency band. These blocks, shown in Fig. 14(b), contain only the RWG paths in Fig. 9 and not the SIW in PCB. These measurements serve as a way to distinguish the different losses in this prototype and to validate the LPF.

Fig. 14(a) shows the WR-10 RWG results. A minor discontinuity at 90 GHz corresponds to the transition between measurement setups. In the passband (60–90 GHz), the measured IL ranges from 0.8 to 1.6 dB, which is slightly lower than simulated values. The return loss (RL) is slightly degraded, and some resonances appear in the stopband (>100 GHz), likely due to manufacturing tolerances. Nevertheless, the transmission coefficient in this band is mostly below −30 dB, showing good blockage of signals in the high-band.

Fig. 14(c) presents the WR-8 band results. The observed IL in the high-band ranges between 0.6 and 1.9 dB. The reflection coefficient trend matches simulations, though there is a larger ripple in the measurement in the high-band. Nevertheless, the

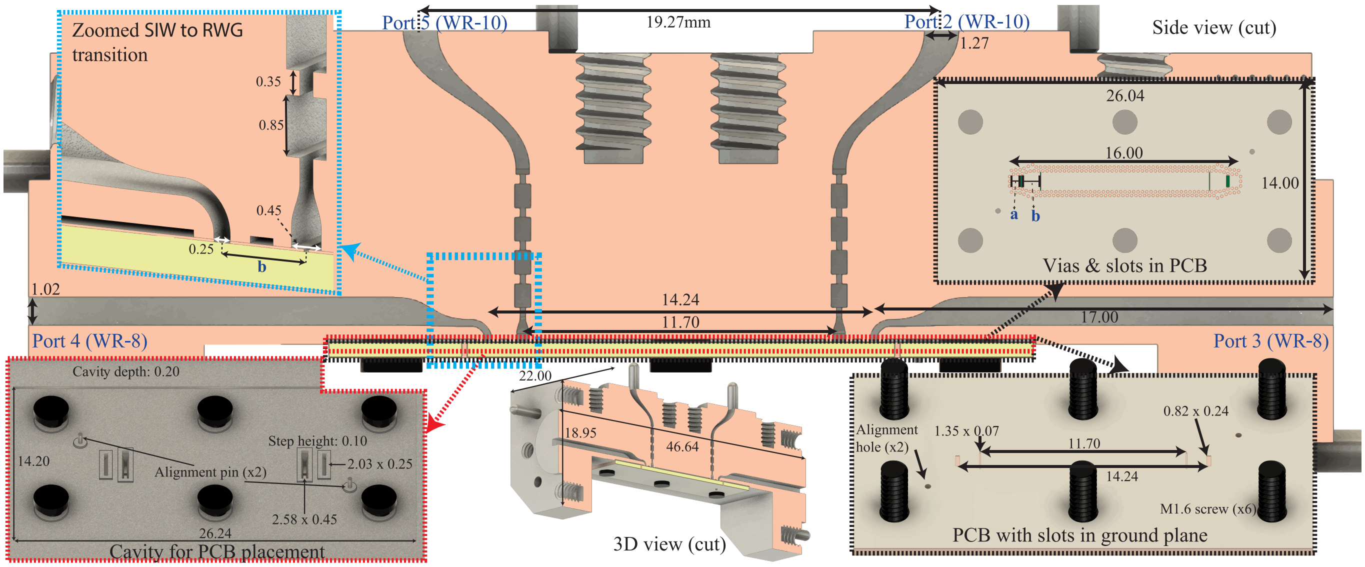

Fig. 12. Schematic of the B2B prototype (Step 6 of design procedure in Fig. 4) highlighting several parts of the design. Separate insets highlight a 3-D perspective view of the SIW to RWG transition (in blue), the cavity in which the PCB is placed and attached to the metal block (in red), a cut of the 3-D view of the whole FST, and finally the top and bottom of the PCB showing the slots and vias in the SIW (in the black outlines). All dimensions in mm.

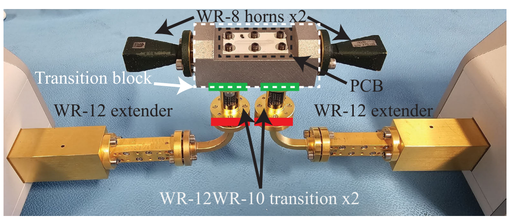

(a) Setup for WR-10 using WR-12 extenders. Transitions are attached to the prototype to taper from WR-10 to WR-12. The green line in highlights the normalization plane due to the lack of a WR-10 calibration kit.

(b) Setup for WR-8.

Fig. 13. Measurement setups to characterize the FST for the WR-10 band in (a) and WR-8 band in (b). Horn antennas are used as a matched load to terminate the open WG ports into absorbers. The red lines indicate the calibration plane used for these setups.

reflection coefficient remains below −16 dB in the high-band. The lower frequency cutoff has shifted slightly to a lower frequency, probably caused by the RWG dimensions being slightly larger than simulated.

C. Transition Block

The full FST structure, integrating the SIW-to-RWG interface and frequency-splitting functionality, was evaluated using seven PCBs to assess assembly sensitivity. Fig. 15(a) shows the WR-10 port performance. A working band is observed around 80 GHz, with transmission close to simulated values of −4 dB. However, the reflection coefficient is shifted, with a narrower BW of only 3.3 GHz compared to the 8.8 GHz that was simulated.

Fig. 15(b) shows the WR-8 port results. Here, a significant mismatch is observed in the matching, primarily due to deviations in the slot dimensions near the transition. Although the slots were designed to be 250 μm wide, microscope measurements revealed widths up to 400 μm. As shown in Fig. 16, the slots also exhibit rough edges and a deformed sidewall, further deteriorating the performance. Despite these issues, the transmission around 130 GHz remains functional, with an IL of approximately 5 dB in the B2B configuration, similar to the performance in the low-band and out-performing alternatives like solder balls [5] and bondwires [6].

To assess the isolation and overall performance of the dual-band transition, the full S-matrix was measured and is shown in Fig. 17 (reflection coefficients) and Fig. 18 (transmission coefficients). These measurements are performed for just a single PCB. To execute these measurements, the setups in Fig. 13 were adopted with additional transitions (WR-10 to WR-8 and WR-10 to WR-12) for proper matching. For some cases, calibration at the DUT ports was not possible due to different RWG-sizes. For example, measuring the isolation between Port 2 (WR-10) and Port 3 (WR-8). In these cases, the losses were normalized and corrected for in postprocessing. As for the reflection coefficients, the closest possible calibration plane was used, which often resulted in one or two taper transitions not being included in the calibration. As for the reflection coefficients of these taper transitions, they were deemed to be high enough to neglect.

In the low band, the isolation between channels is at least 10 dB, achieved only by employing below-cutoff RWG and SIW sections as seen in Fig. 12. However, due to the over-sized high-frequency RWGs (see Fig. 16), the isolation is lower than the simulated 20 dB. This effect is amplified by the fact that the low band was operating very close to, but over, the cut-off frequency of the WR-8 RWG, which is

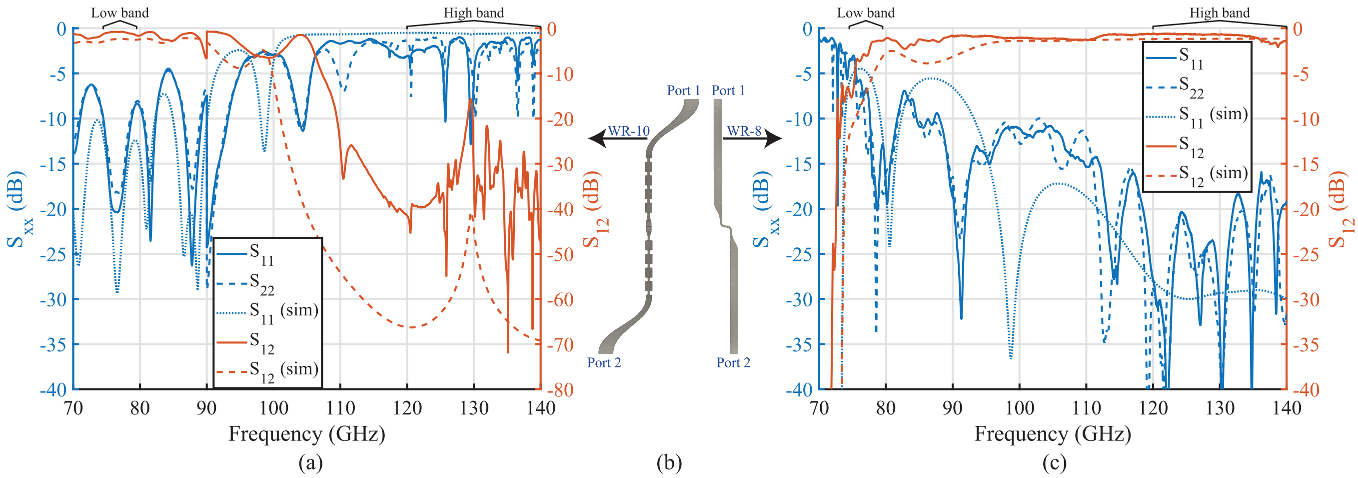

Fig. 14. (a)–(c) Measurements and simulation for B2B WR-10 RWG and B2B WR-8 RWG blocks, respectively. Both low-band (60–90 GHz) and high-band (90–140 GHz) performance is shown. The B2B RWG blocks are shown in (b). Due to symmetry, only one simulated reflection coefficient is plotted.

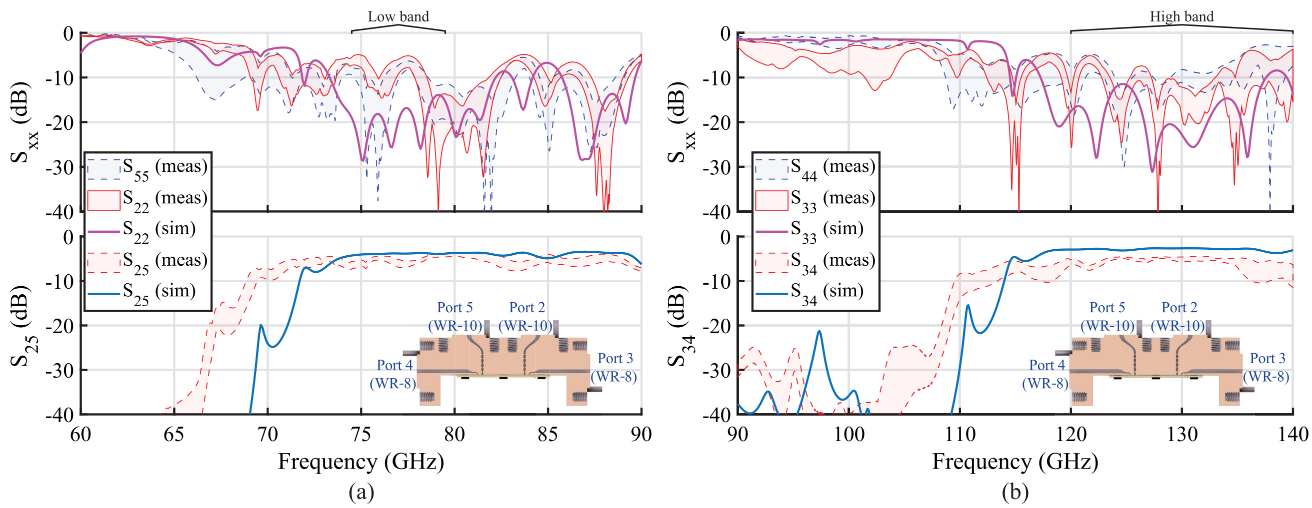

Fig. 15. (a) and (b) Measurements and simulation for the WR-10 and WR-8 port of the transition block in Fig. 12, respectively. The shaded area depicts the result range over the seven measured PCBs. Due to symmetry, only one simulated reflection coefficient is plotted.

73.77 GHz. A slight shift of this size results in a significantly smaller attenuation effect. In the high band, the measured isolation exceeds 30 dB, though simulations predicted values above 50 dB. The reduced isolation is attributed to manufacturing deviations, particularly in the slot geometry. The interoutput isolation S_{23}, S_{54}, S_{24}, and S_{53} follow a similar trend compared to S_{23} in Fig. 8.

VI. Discussion

The results presented in Section V demonstrate the feasibility of the proposed dual-band SIW-to-RWG FST. However, several practical limitations were observed, primarily stemming from the manufacturing process and its impact on critical dimensions.

A. Discrepancy Analysis

While the use of LPBF additive manufacturing enabled rapid prototyping and integration of complex 3-D mmWave structures at a competitive cost of approximately €1000 for a B2B block, the technology still faces challenges in achieving the dimensional precision required for mmWave applications. In particular, the slot widths at the transition interface, arguably the most critical region, exhibited deviations of up to 60% from the intended 250 μm, as shown in Fig. 16. These deviations led to significant impedance mismatches and increased IL, especially in the WR-8 band.

In order to find the discrepancies between the measurements and the simulations, some of the deviations found in the prototype were implemented into the simulation model. First, the slot dimensions were altered to match the measured dimensions in Fig. 16. Second, a misalignment and a bend were introduced in the PCB. In the prototype, it was observed that even though the contact area was reduced, the surface was still not completely flat, resulting in a slightly warped PCB after assembly. Also, by analyzing microscope images, the SR was determined. Near the outside edges of the transition, the critical part of this design, the SR (rms), was found to be 21 μm, while 4 μm was expected. Furthermore, the SR (rms) inside the low-band RWG was found to be roughly

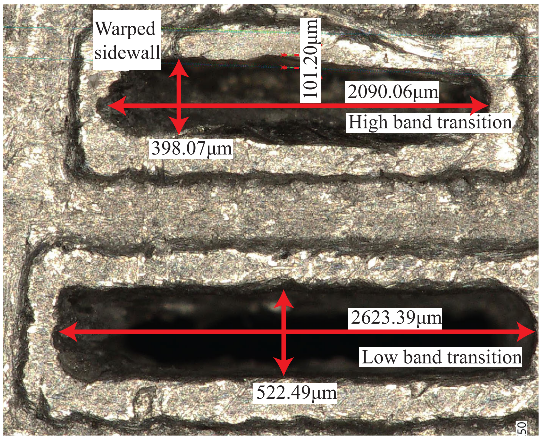

Fig. 16. Microscope image of transition slots on prototype showing deviation and rough edges. Moreover, a deformed side wall can be seen on the high-frequency slot (right).

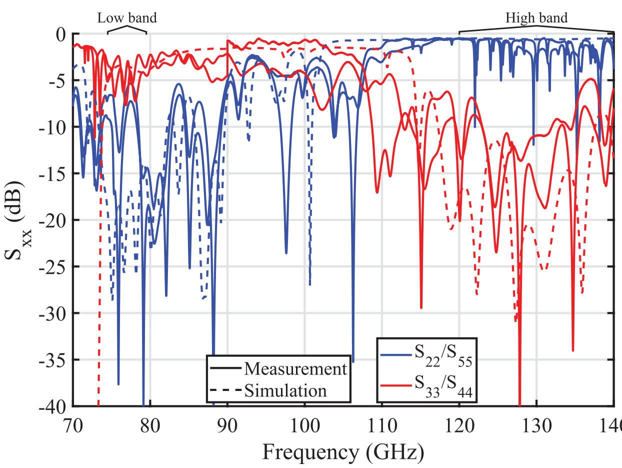

Fig. 17. Measurements and simulation for reflection coefficients of both ports over the whole frequency band.

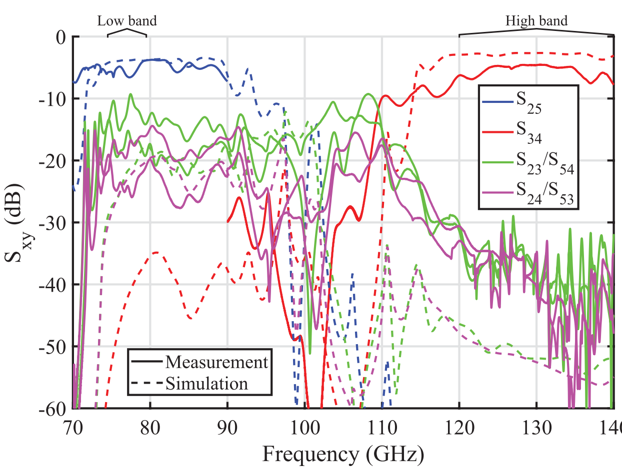

Fig. 18. Measurements and simulation for transmission coefficients of both ports over the whole frequency band.

11 μm, which remains relatively rough. However, the B2B RWG measurements in Fig. 14 resulted in lower losses than expected, possibly indicating that the surface roughness (SR) is not an issue for these designs. This might indicate that, especially at the transition, smooth walls are hard to achieve. It will be beneficial to study how to implement these location-dependent SR inside the simulation model. In CST, the SR is modeled as a random process with a normal distribution using the provided SR value. This should be considered when the SR (rms) is larger than 0.5δ where δ is the skin depth described by $\delta = (\rho/\pi f \mu)^{1/2}$, where ρ is the resistivity of the material (9.01 $\mu\Omega$-cm in our setup [31]), f is the frequency, and μ is the permeability of the material. In our prototype, 0.5δ corresponds to 0.27 μm at 77 GHz and 0.21 μm at 130 GHz, both far below the measured SR levels, indicating that conductor roughness can contribute to excess loss at both frequencies. Importantly, the roughness sensitivity is expected to increase with frequency because δ decreases at 130 GHz. However, in this prototype SR $\gg \delta$ in both bands, placing the structures in a strongly rough regime where the incremental change from 77 to 130 GHz is comparatively small relative to geometry-induced mismatch effects. Therefore, in the present prototype, the measurement discrepancy is expected to be dominated by geometry-induced mismatches (altered slot dimensions), while a refined, location-dependent roughness model is left for future work.

The updated simulations, taking into account the altered slot dimensions and a misalignment and bend in the PCB, are shown together with the measurements and old simulations in Fig. 19 for WR-10 and WR-8. As can be seen, there is more correlation between the measurements and simulations than before. In both the updated low- and high-band simulations, the RL behavior is closer to what is seen in the measurement data. Furthermore, especially in the high band [Fig. 19(b)] the new simulated S_{34} is closer to the measured value. However, not all deviations can be accounted for because some features are not reachable by conventional measurement. Potentially, a more detailed analysis, like an X-ray, of this design can show these potential deviations in more detail.

B. Comparison With Previous Work

Table I summarizes key measured performance metrics from recent literature on SIW-to-RWG transitions. While most of the designs utilize CNC-milling, this work uses metal-only additive manufacturing, allowing more design freedom.

Furthermore, most prior works focus on single-band transitions and do not address the integration of frequency-splitting. To the author's best knowledge, this article is the only one to address such a high frequency for a FST. For example, [16], [17], and [33] report low-loss transitions using transverse coupling and gap-WG techniques, but these require complex assembly and are not easily scalable to dual-band systems. The vertical transition approach used in this work offers better mechanical robustness and integration potential. While the measured IL of 0.8–1.6 dB (WR-10) and 0.6–1.9 dB (WR-8) for the RWG B2B blocks is competitive, the full transition structure exhibited higher losses due to the aforementioned deviations in fabricating the slots. Furthermore, comparing the isolation to [11] and [12] shows worse performance. However, these designs operate at frequencies below 32 GHz and focus on the diplexing behavior rather than on the transition. More-

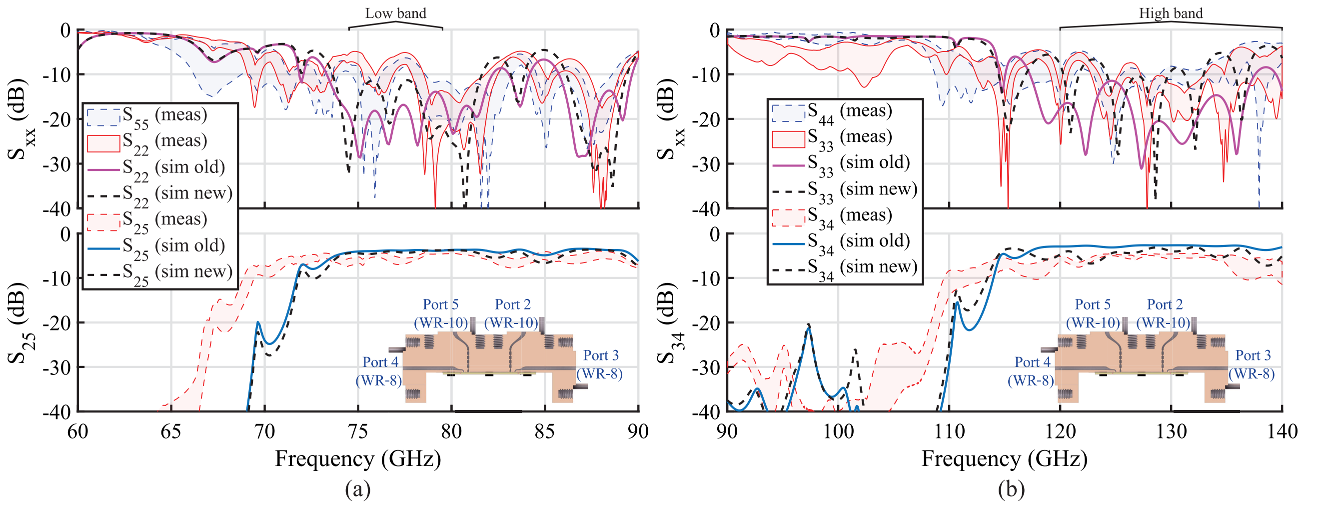

Fig. 19. (a) and (b) Updated simulation taking into account manufacturing effects, compared to original simulation and measurements for the WR-10 and WR-8 bands, respectively. The updated simulations show a closer match to the measured values. The shaded area depicts the result range over the seven measured PCBs.

TABLE I
COMPARISON WITH PREVIOUSLY PUBLISHED DESIGNS

Ref.	Band (GHz)	RL (dB)	IL (dB) (single)	Frequency-selective	Isolation (dB)	Transverse size (λ_0^1 x λ_0)	Transition type	Manufacturing Technology
[12]	19.2 – 20.4 29 – 30.4	≥ 10 ≥ 10	≤ 1.1 ≤ 1.3	yes	≥ 42 ≥ 32	0.58 x 0.50	Orthogonal diplexer and power splitter using resonant patches and ridge WG	PCB and CNC-milling
[11]	20.2 – 20.8 29 – 31	≥ 10 ≥ 10	≤ 1.7 ≤ 1.7	yes	≥ 25 ≥ 28	0.62 x 0.68	Orthogonal diplexer using a resonant patch and ridge WG	PCB and CNC-milling
[32]	24.5 – 37.8	≥ 10	< 0.3	no	-	0.27 x 0.24	Orthogonal. Aperture to stepped ridge WG	PCB and CNC-milling
[9]	54 – 72[2]	≥ 12	≤ 0.58	no	-	1.04 x 0.75	Orthogonal. Slot to slot-coupled rectangular patch	PCB and off-the-shelf coax to RWG launcher
[33]	72 – 95.5	≥ 10	≤ 0.7	no	-	1.35 x 0.34	Transverse. Microstrip to SIW to ridge WG	PCB and CNC-milling
[17]	80 – 114	≥ 13	≤ 0.4	no	-	0.65 x 0.65	Transverse. Cavity with probe	CNC-milling (gap-wave)
[16]	84.5 – 108	≥ 9.5	≤ 0.75	no	-	0.6 x 0.47	Transverse. SIW to ridge gap WG	GaAs and CNC-milling (gap-wave)
This paper	78.5 – 81.8 123.3 – 133.9	≥ 10 ≥ 7	≤ 2.9 ≤ 2.95	yes	≥ 10 ≥ 30	0.75 x 0.70	Orthogonal FST with E-plane bend and slot-coupled SIW to RWG T-junction	PCB and Metal-only 3D printing (LPBF)

[1] Center of measured low band for dual-band designs
[2] Limited by VNA frequency range

over, increasing the isolation in the low-band of the present design is possible by using a HPF, as previously discussed.

C. Design Improvements and Future Work

The current design relies on WG cut-off behavior for band separation in the high-frequency path. While this approach simplifies the structure, it also limits isolation performance. As shown in Fig. 18, the measured isolation in the low band was at least 10 dB, which is significantly lower than the simulated 20 dB. To improve this, a dedicated HPF could be added to the 130-GHz path, improving the isolation to over 30 dB, similar to the LPF implemented for the 77-GHz channel (see Section IV). Moreover, the RWG could deviate from the standard WR-8 interface. Simulations have shown that by decreasing the width of the RWG by 0.3 mm, the isolation can be improved by roughly 18 dB while the matching in the high-band only deteriorates slightly.

Even though micromilling would require split-block assembly, it might be interesting to investigate for FST manufacturing. Although more costly and time-consuming, such methods offer superior dimensional control and surface finish, which are critical for high-frequency transitions.

Moreover, the sensitivity analysis in Fig. 11 highlighted the importance of precise PCB alignment. Although the alignment pins were included in the design, further improvements in mechanical stability and assembly procedures could help reduce variability across prototypes. Alternatively, conductive adhesive paste could be used to better bond the PCB to the metal package and ensure proper contact.

Finally, the integration of active components and antenna arrays will be investigated to demonstrate full system-level performance.

VII. Conclusion

This article presented a novel dual-band SIW-to-RWG FST, targeting future automotive radar systems operating at 77 and 130 GHz. To the author's best knowledge, this is the first FST reported in the literature for these frequencies. The proposed structure enables compact and efficient routing from a single BFIC to two separate antenna arrays as shown in Fig. 1, leveraging WG-based filtering and metal-only additive manufacturing for high-frequency integration.

Experimental results confirmed the feasibility of the concept, with measured ILs of 0.8–1.6 dB (WR-10) and 0.6–1.9 dB (WR-8) for the RWG blocks. However, deviations in critical dimensions, particularly the coupled slot widths at the transition interface, led to increased mismatch and reduced isolation in the full transition structure, resulting in a single-ended IL around 2.5 dB for both bands.

Despite the observed limitations, the measured results validate the core design concept and integration: a compact, dual-band transition structure that enables efficient routing from a single BFIC to two separate antenna arrays. The architecture supports a future extension to joint communication and sensing (JCAS), where radar and communication systems are co-designed to share hardware, spectrum, and signal processing resources. By enabling dual-band operation within a compact, monolithic package, the proposed solution addresses key challenges in JCAS implementation such as minimizing IL, reducing system complexity, and supporting high-resolution sensing alongside robust communication.

Acknowledgment

The authors would like to thank Northern Waves AB [28] for manufacturing the prototype and for their expertise in the realization of this design. Finally, they thank Paola Escobari for her input on SR determination and effects.

References

[1] K. Moerman, A. Pandharipande, W. Rouwet, and M. Tomesen, "6G communications and mobility," NXP, The Netherland, Tech. Rep., 2022. [Online]. Available: https://www.nxp.com/docs/en/data-sheet/SEC-LEVEL-0-SA.pdf

[2] A. Filippi, V. Martinez, and M. Vlot, "Spectrum for automotive radar in the 140 GHz band in Europe," in *Proc. 19th Eur. Radar Conf. (EuRAD)*, Sep. 2022, pp. 1–4. [Online]. Available: https://ieeexplore.ieee.org/document/9924643

[3] *140 GHz Radar: Smarter, Safer Cars Within Everyone's Reach*. Accessed: Feb. 13, 2026. [Online]. Available: https://www.imec-int.com/en/articles/high-resolution-low-cost-140-ghz-radar-bringing-smarter-safer-cars-\break within-everyones-reach

[4] M. Murad, J. Nickolaou, G. Raz, J. S. Colburn, and K. Geary, "Next generation short range radar (SRR) for automotive applications," in *Proc. IEEE Radar Conf.*, May 2012, pp. 0214–0219. [Online]. Available: https://ieeexplore.ieee.org/document/6212139

[5] B. A. Thrasher, "A 10 MHz to 80 GHz low-temperature cofired ceramic ball grid array board-to-interposer transition for chip scale packages," *J. Ceramic Sci. Technol.*, vol. 6, no. 4, pp. 279–284, 2015, doi: 10.4416/JCST2015-00054.

[6] T. Krems, W. Haydl, H. Massler, and J. Rudiger, "Millimeter-wave performance of chip interconnections using wire bonding and flip chip," in *IEEE MTT-S Int. Microw. Symp. Dig.*, vol. 1, Jun. 1996, pp. 247–250. [Online]. Available: https://ieeexplore.ieee.org/document/508504

[7] A. Aljarosha, P. Kaul, A. B. Smolders, M. K. Matters-Kammerer, and R. Maaskant, "Silicon-based IC-waveguide integration for compact and high-efficiency mm-Wave spatial power combiners," *IEEE Trans. Compon., Packag., Manuf. Technol.*, vol. 11, no. 7, pp. 1115–1121, Jul. 2021. [Online]. Available: https://ieeexplore.ieee.org/document/9446879

[8] L. Li, X. Chen, R. Khazaka, and K. Wu, "A transition from substrate integrated waveguide (SIW) to rectangular waveguide," in *Proc. Asia Pacific Microw. Conf.*, Dec. 2009, pp. 2605–2608. [Online]. Available: https://ieeexplore.ieee.org/abstract/document/5385245

[9] Y. Li and K.-M. Luk, "A broadband V-band rectangular waveguide to substrate integrated waveguide transition," *IEEE Microw. Wireless Compon. Lett.*, vol. 24, no. 9, pp. 590–592, Sep. 2014. [Online]. Available: https://ieeexplore.ieee.org/document/6848864

[10] A. Hosseini-Fahraji, K. Mohammadpour-Aghdam, and R. Faraji-Dana, "Millimeter wave rectangular waveguide to grounded CPW transition on multi-layer substrate," in *Proc. 4th Int. Conf. Millim.-Wave THz Technol. (MMWaTT)*, Dec. 2016, pp. 99–102. [Online]. Available: https://ieeexplore.ieee.org/document/7869926

[11] K. Erkelenz, L. P. P. B. Bohl, A. Sieganschin, and A. F. Jacob, "A compact K-/Ka-band rectangular-to-coplanar waveguide transition with integrated diplexer," *IEEE Microw. Wireless Compon. Lett.*, vol. 31, no. 6, pp. 642–645, Jun. 2021. [Online]. Available: https://ieeexplore.ieee.org/document/9373336

[12] K. Erkelenz, L. Meyer, N. Sielck, B. Deutschmann, and A. F. Jacob, "A compact K-/Ka-band waveguide transition with integrated diplexer and power divider," in *Proc. 51st Eur. Microw. Conf. (EuMC)*, Apr. 2022, pp. 95–98. [Online]. Available: https://ieeexplore.ieee.org/document/9784180

[13] K. A. P. Van Hastenberg, M. V. Ivashina, A. B. Smolders, and A. R. Vilenskiy, "Novel dual-band SIW-to-metal waveguide transition with integrated filtering for diplexing 77 GHz and 130 GHz frequency bands," in *Proc. 19th Eur. Conf. Antennas Propag. (EuCAP)*, Mar. 2025, pp. 1–5. [Online]. Available: https://ieeexplore.ieee.org/document/10999541

[14] A. Ali, M. N. Awan, W. A. Malik, S. Y. Chaudhry, Hidayatullah, and J. Haider, "A compact and high gain X/Ku band shared aperture antenna array with enhanced inter-band and cross-band isolation," *IEEE Access*, vol. 12, pp. 146137–146146, 2024. [Online]. Available: https://ieeexplore.ieee.org/document/10540089

[15] M. Ihle, S. Ziesche, C. Zech, and B. Baumann, "Functional printing of MMIC-interconnects on LTCC packages for sub-THz applications," in *Proc. 22nd Eur. Microelectron. Packag. Conf. Exhib. (EMPC)*, Sep. 2019, pp. 1–4. [Online]. Available: https://ieeexplore.ieee.org/document/8951799

[16] A. R. Vilenskiy and Y. Zhang, "A compact and wideband MMIC to ridge gap waveguide contactless transition for phased array antenna front-ends," *IEEE Antennas Wireless Propag. Lett.*, vol. 23, no. 3, pp. 990–994, Mar. 2023. [Online]. Available: https://ieeexplore.ieee.org/abstract/document/10349922

[17] A. U. Zaman, V. Vassilev, H. Zirath, and N. Rorsman, "Novel low-loss millimeter-wave transition from waveguide-to-microstrip line suitable for MMIC integration and packaging," *IEEE Microw. Wireless Compon. Lett.*, vol. 27, no. 12, pp. 1098–1100, Dec. 2017. [Online]. Available: https://ieeexplore.ieee.org/document/8100625

[18] D. Zhang, Z. Xu, Y. Xiao, and H. Sun, "A wideband siw-to-waveguide transition at w-band," in *Proc. 6th Asia Pacific Conf. Antennas Propag. (APCAP)*, Oct. 2017, pp. 1–3. [Online]. Available: https://ieeexplore.ieee.org/document/8420609

[19] R. K. Chandan, A. K. Singh, and S. Pal, "A low cost, mmWave waveguide-to-strip line transition for 5G applications," in *IEEE MTT-S Int. Microw. Symp. Dig.*, Dec. 2021, pp. 1–3. [Online]. Available: https://ieeexplore.ieee.org/document/9714706

[20] C.-M. Hung, C.-F. Jheng, K.-Y. Lee, C.-I.-G. Hsu, and M.-H. Ho, "Dual-band filter and diplexer design using extremely miniaturized substrate-integrated coaxial cavity," *Sensors*, vol. 25, no. 9, p. 2921, May 2025. [Online]. Available: https://www.mdpi.com/1424-8220/25/9/2921

[21] K. Huang, W. Li, H. Zeng, Y. Zhang, and Z. Yang, "A D-band wideband high isolation diplexer," in *Proc. 5th China Int. Young Scientist THz Conf.*, 2024, pp. 108–112.

[22] D. F. Williams, J. Jargon, U. Arz, and P. Hale, "Rectangular-waveguide impedance," in *Proc. 85th Microw. Meas. Conf. (ARFTG)*, May 2015, pp. 1–5. [Online]. Available: https://ieeexplore.ieee.org/document/7162902

[23] Y. Cassivi, L. Perregrini, P. Arcioni, M. Bressan, K. Wu, and G. Conciauro, "Dispersion characteristics of substrate integrated rectangular waveguide," *IEEE Microw. Wireless Compon. Lett.*, vol. 12, no. 9, pp. 333–335, Sep. 2002. [Online]. Available: https://ieeexplore.ieee.org/document/1031925

[24] B. F. Zong, H. Y. Zeng, and F. Wu, "Field distributions analyzed of substrate integrate waveguide (SIW)," *Proc. Comput. Sci.*, vol. 166, pp. 241–247, Jan. 2020. [Online]. Available: https://www.sciencedirect.com/science/article/pii/S1877050920302283

[25] I. A. Eshrah, A. A. Kishk, A. B. Yakovlev, and A. W. Glisson, "Generalized equivalent circuit model for transverse waveguide slots and applications," *Prog. Electromagn. Res.*, vol. 69, pp. 1–20, 2007. [Online]. Available: http://www.jpier.org/PIER/pier.php?paper=06110803

[26] D. M. Pozar, *Microwave Engineering*, 4th ed., Hoboken, NJ, USA: Wiley, Nov. 2011. [Online]. Available: https://www.wiley.com/en-us/Microwave

[27] (Jul. 2023). *CST Studio Suite*. [Online]. Available: https://www.3ds.com/products/simulia/cst-studio-suite

[28] *Northern Waves*. Accessed: Feb. 26, 2025. [Online]. Available: https://northern-waves.com/

[29] *Surface Roughness in 3D Printing*. [Online]. Available: https://xometry.pro/en-eu/articles/3d-printing-surface-roughness/

[30] Keysight. *Advanced Design System*. Accessed: Feb. 13, 2026. [Online]. Available: https://www.keysight.com/us/en/products/software/pathwave-design-software/pathwave-advanced-design-system.html

[31] C. Silbernagel, I. Ashcroft, P. Dickens, and M. Galea, "Electrical resistivity of additively manufactured $AlSi_{10}Mg$ for use in electric motors," *Additive Manuf.*, vol. 21, pp. 395–403, May 2018. [Online]. Available: https://www.sciencedirect.com/science/article/pii/S2214860418300769

[32] A. Roev, P. Taghikhani, R. Maaskant, C. Fager, and M. V. Ivashina, "A wideband and low-loss spatial power combining module for mm-wave high-power amplifiers," *IEEE Access*, vol. 8, pp. 194858–194867, 2020. [Online]. Available: https://ieeexplore.ieee.org/document/9239291

[33] A. Aljarosha, A. U. Zaman, and R. Maaskant, "A wideband contactless and bondwire-free MMIC to waveguide transition," *IEEE Microw. Wireless Compon. Lett.*, vol. 27, no. 5, pp. 437–439, May 2017. [Online]. Available: https://ieeexplore.ieee.org/document/7911264

Kevin A. P. van Hastenberg (Graduate Student Member, IEEE) was born in Sint-Oedenrode, The Netherlands, in 1999. He received the B.Sc. and M.Sc. (Hons.) degrees in electrical engineering from Eindhoven University of Technology (TU/e), Eindhoven, The Netherlands, in 2020 and 2022, respectively, where he is currently pursuing a Ph.D. degree with a specialization in shared apertures for 6G communication and radar sensing.

During his M.Sc., he was part of the NXP Fellowship Program focusing on mmWave technology. In 2021, he finalized his M.Sc. degree by investigating an antenna array with flexible (satellite) communication capabilities. Furthermore, he was a Visiting Student with The Netherlands Foundation for Research in Astronomy (ASTRON), Dwingeloo, The Netherlands, where he performed a preliminary study on a wide field-of-view telescope for sciences at 5 GHz. In 2024, he was a Secondment at the Chalmers University of Technology, Gothenburg, Sweden.

Marianna V. Ivashina (Senior Member, IEEE) received the Ph.D. degree in electrical engineering from Sevastopol National Technical University (SNTU), Sevastopol, Ukraine, in 2001.

From 2001 to 2010, she was with The Netherlands Institute for Radio Astronomy (ASTRON), Dwingeloo, The Netherlands, where she carried out research on innovative phased array technologies for future radio telescopes, such as the Square Kilometer Array. In 2002 and 2003, she was a Visiting Scientist with the European Space Agency, ESTEC, Noordwijk, The Netherlands, where she studied multiple-beam array feeds for the satellite telecommunication system large deployable antenna. In January 2011, she joined Chalmers University of Technology, Gothenburg, Sweden, where she is currently a Full Professor and the Head of the Antenna Systems Group with the Department of Electrical Engineering. She has published extensively on the above topics, having authored/co-authored over 130 journal and conference papers. Her current research interests include antenna array systems, integration of antennas with active electronic components, synthesis of aperiodic arrays, and other unconventional array architectures, reflector antennas, and focal plane array feeds.

Prof. Ivashina has received several scientific awards [including the URSI Young Scientists Award for GA URSI, Toronto, Canada, in 1999, the APS/IEEE Travel Grant, Davos, Switzerland, in 2000, the "Best team contribution" Paper Award from the ESA Antenna Workshop in 2008, the EU FP7 Marie Curie Actions International Qualification Fellowship in 2009, the Best Paper Award from the IEEE COMCAS Conference, Tel-Aviv, Israel, in 2019], and numerous research project funding grants from Swedish and European funding agencies. She was an Associate Editor of IEEE TRANSACTIONS ON ANTENNAS AND PROPAGATION and is currently a Board Member of the European School of Antennas (ESoA). Since 2021, she has been the Delegate of the European Association of Antennas and Propagation (EurAAP) for Region 6: Iceland, Norway, and Sweden.

A. Bart Smolders (Senior Member, IEEE) was born in Hilvarenbeek, The Netherlands, in 1965. He received the M.Sc. and Ph.D. degrees in electrical engineering from Eindhoven University of Technology (TU/e), Eindhoven, The Netherlands, in 1989 and 1994, respectively.

From 1989 to 1991, he worked as an MMIC Designer at FEL-TNO, The Hague, The Netherlands. From 1994 to 1997, he was a Radar System Designer with Thales Group, Thales, The Netherlands. From 1997 to 2000, he was the Project Leader of the Square Kilometer Array (SKA) with Netherlands Foundation for Research in Astronomy (ASTRON), Dwingeloo, The Netherlands. From 2000 to 2010, he has been with NXP (formerly Philips) Semiconductors, Eindhoven, responsible for innovation in the RF business line. Since 2010, he has been a Full-Time Professor with TU/e in the Electromagnetics Group with special interest in antenna systems and applications. He currently leads several research projects in the area of integrated antenna systems operating at frequencies up to 300 GHz for several application domains, including 5G/6G wireless communications, radar sensors, and radio astronomy.

Dr. Smolders is one of the Co-Founders of the FNS-6G growth-fund project and also the start-up company ANTENNEX. Currently, he is the Chair of the EuRAAP Workgroup on Active Antenna Arrays and an Organizer of the 6G Forum at EuMW 2025. He is the Chair of the Stichting Wetenschappelijke Activiteiten van het Nederlands URSI Committee (SWAN). He was the Chair of the IEEE Benelux section and the Chair of the Nederlands Radio- en Elektronica Genootschap (NERG). Next to his research activities, he was the Dean of the Electrical Engineering Department, TU/e, from 2016 to 2023. He has authored more than 250 papers. More details can be found at: https://www.tue.nl/en/research/researchers/bart-smolders/

Artem R. Vilenskiy (Senior Member, IEEE) received the M.Sc. degree (summa cum laude) in radio engineering and the Ph.D. degree in antennas and microwave devices from Bauman Moscow State Technical University, Moscow, Russia, in 2011 and 2014, respectively.

From 2011 to 2019, he was with the Samsung Research Institute Russia, Moscow, Russia, where he had roles of a Researcher, an Expert Engineer, and the Project Leader at the Electromagnetics Group and RF Sensor Part. From 2015 to 2019, he was a Visiting Associate Professor at the Radio-Electronic Systems and Devices Department, Bauman Moscow State Technical University. From 2019 to 2024, he was a Researcher with the Antenna Systems Group, Chalmers University of Technology, Gothenburg, Sweden. He is currently a Microwave Team Lead at XPANCEO, Dubai, United Arab Emirates. His research interests include applied and computational electromagnetics, antenna and front-end integrated circuit design, and controllable high-frequency materials and devices.